

Canals beyond Mars: Beam depolarization in radio continuum maps of the warm ISM

M. Haverkorn^{1,2} and F. Heitsch^{3,4,5}

¹ Sterrewacht Leiden PO Box 9513, 2300 RA Leiden, The Netherlands

² Harvard-Smithsonian Center for Astrophysics, 60 Garden Street MS-67, Cambridge, MA, 02138, USA

³ Max-Planck-Institut für Astronomie, Königstuhl 17, 69117 Heidelberg, Germany

⁴ University of Wisconsin-Madison, 475 N Charter St, Madison, WI 53706, USA

⁵ Institut für Astronomie und Astrophysik, Universität München, Scheinerstr. 1, 81679 München, Germany
e-mail: heitsch@usm.uni-muenchen.de

Received 5 October 2003 / Accepted 8 March 2004

Abstract. Multi-frequency radio polarimetric observations of the diffuse Galactic synchrotron background enable us to study the structure of the diffuse ionized gas via rotation measure maps. However, depolarization will introduce artifacts in the resulting rotation measure (RM), most notably in the form of narrow, elongated “depolarization canals”. We use numerical models of a non-emitting Faraday rotating medium to study the RM distribution needed to create depolarization canals by depolarization due to a finite beam width, and to estimate the influence of this depolarization mechanism on the determination of RM. We argue that the depolarization canals indeed can be caused by beam depolarization, which in turn is a natural consequence when observing a turbulent medium with limited resolution. Furthermore, we estimate that beam depolarization can induce an additional error of about 20% in RM determinations, and considerably less in regions that are not affected by depolarization canals.

Key words. magnetohydrodynamics – magnetic fields – polarization – turbulence – ISM: magnetic fields – radio continuum: ISM

1. Introduction

The Galactic magnetic field and turbulence play a major rôle in structuring the Galactic disk. The recognition of the dynamical importance of turbulence in the interstellar medium (ISM) (e.g., Armstrong et al. 1995) allowed our picture of the ISM to evolve from a simple three-phase gas to a highly complex medium. Turbulence is believed to play a crucial rôle in molecular cloud and star formation (see e.g., Larson 1981; Mac Low & Klessen 2003), however, its origin is widely debated. On a larger scale turbulence leads to chemical mixing (de Avillez & Mac Low 2002) and contributes to the vertical pressure balance in the Galactic disk and to the heating of the ISM (Minter & Balser 1998).

Magnetic fields are tightly linked to the turbulent nature of the ISM. Their large-scale components help confine cosmic rays to the Galaxy, and thus affect chemical processes in molecular clouds. They probably contribute to generating turbulence in the disk (Sellwood & Balbus 1999) and definitely affect the vertical disk structure. The ratio between mass and magnetic flux in the ISM is an essential piece of information necessary

to understand the rôle of magnetic fields in molecular cloud and eventually star formation (see e.g., Crutcher 1999).

Density and magnetic field structure in the ISM can be probed using multi-frequency radio polarimetry to study Faraday rotation¹ in the magneto-ionic medium. Polarized extragalactic point sources and pulsars have been used to determine rotation measures (RM), but these give only measurements at certain lines of sight. Observing the diffuse Galactic synchrotron background instead yields structure in polarized emission on many scales, along many contiguous lines of sight. However, depolarization complicates the interpretation of the resulting RM maps. Depolarization occurs if the telescope beam is larger than the scale of structure in polarization (beam depolarization), along the line of sight if the radiation is emitted and Faraday rotated largely in the same medium (depth depolarization or internal Faraday dispersion), or if the frequency

¹ Faraday rotation is the rotation of the plane of linear polarization of radiation when it propagates through a magneto-ionic medium, due to the birefringence of the medium to circularly polarized radiation. The rotation of the polarization plane through the medium is $\Delta\phi = RM\lambda^2$, with rotation measure $RM = 0.81 \int B_{\parallel} n_e ds$, where B_{\parallel} is the component of the magnetic field parallel to the line of sight in μG , n_e is the thermal electron density in cm^{-3} and ds is the path length in pc.

Send offprint requests to: M. Haverkorn,
e-mail: mhaverkorn@cfa.harvard.edu

bandwidth is so large that the polarization angle changes significantly within the band (bandwidth depolarization), see e.g., Burn (1966) or Sokoloff et al. (1998). In polarization observations of the Galactic synchrotron background, often it is difficult if not impossible to estimate the separate contributions of beam and depth depolarization.

Depolarized regions often exhibit canal-like features (e.g., Duncan et al. 1997, 1999; Gray et al. 1999; Uyaniker et al. 1999; Haverkorn et al. 2000; Gaensler et al. 2001). Both beam and depth depolarization can cause canals, but require a different underlying RM distribution. The goal of this paper is to determine if the observed depolarization canals can be due to beam depolarization, and how beam depolarization affects the computed RM . To this end, we use numerical models of the warm magneto-ionic ISM compared to observations of the diffuse Galactic synchrotron background. The models are irradiated with uniform synchrotron background emission, which is Faraday rotated in the modeled medium. Then, the polarized radiation is smoothed to simulate a finite telescope beam, whereafter RM s are computed from the smoothed emission maps. The structure in polarized intensity and RM emerging from the smoothed modeled radiation field is then compared to the observations. This allows us to simulate the effect that beam depolarization has on polarimetric observations of the ionized ISM.

This work was motivated by the observations briefly presented in Sect. 2. In Sect. 3 we describe the numerical models, the addition of the synchrotron background and the simulation of beam depolarization. Section 4 discusses the signature of beam depolarization in the maps of polarized intensity, while in Sect. 5 the effect of beam depolarization on RM is studied.

2. The observations

The observations were made with the Westerbork Synthesis Radio Telescope (WSRT) in five frequency bands centered on 341, 349, 355, 365, and 375 MHz, each with a bandwidth of 5 MHz. The field discussed here is centered at $(l, b) = (161^\circ, 16^\circ)$ and about 50 square degrees in size, and has a resolution of about $4'$. All four Stokes parameters I , Q , U and V are measured, from which polarized intensity P and polarization angle ϕ were determined as

$$P = \sqrt{Q^2 + U^2}, \quad (1)$$

$$\phi = \frac{1}{2} \arctan \frac{U}{Q}. \quad (2)$$

The instrumental linear polarization is $\lesssim 1\%$. For a detailed description of this field see Haverkorn et al. (2003a).

No signal was detected in total intensity I . As the interferometer is only sensitive to scales smaller than approximately a degree, the non-detection of I means that I does not exhibit any structure on scales smaller than $\sim 1^\circ$, so that the observed total synchrotron power must be very uniform. On the other hand, abundant structure in linearly polarized emission was detected, both in P (see Fig. 1) and in ϕ . This indicates that the small-scale structure in polarization is caused by Faraday rotation and depolarization. Ubiquitously present in the field are one-beam wide ‘‘canals’’ of beam depolarization, which we will

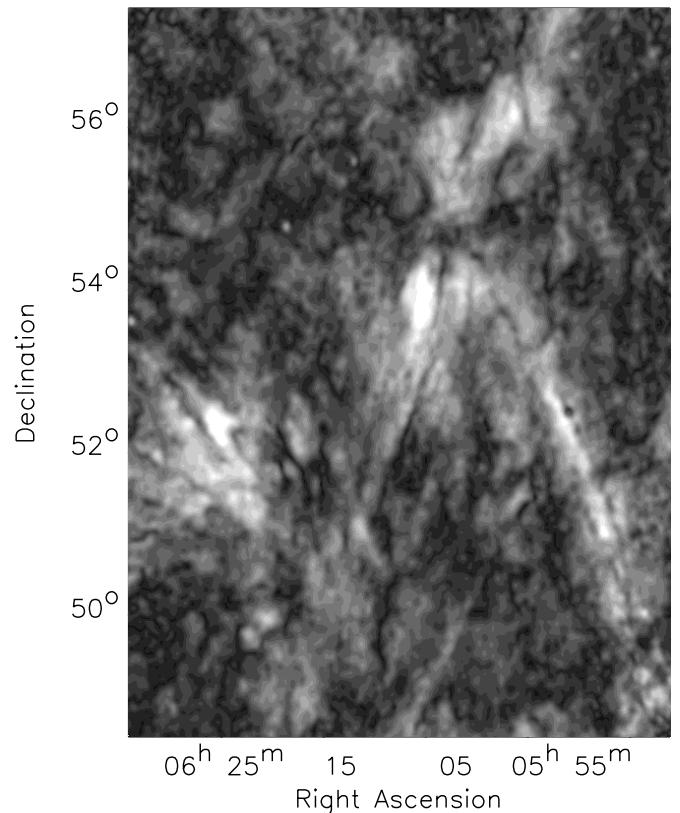


Fig. 1. Observed polarized intensity at 349 MHz in a field centered at $(l, b) = (161^\circ, 16^\circ)$. High intensity is shown white, up to a maximum of ~ 13 K.

discuss in Sect. 4. Missing large-scale structure in P probably does not play a large rôle in this field (Haverkorn et al. 2003a, 2004b).

RM s were computed from linear fits of ϕ against λ^2 . For about 70% of the beams with an average polarized intensity $\langle P \rangle > 5$ S/N, reliable RM 's (with reduced $\chi^2 < 2$) could be determined. This is about 28% of all data. Figure 2 shows a grey scale map of RM , where in each beam a RM value is plotted, regardless of the quality of fit of the $\phi(\lambda^2)$ -relation. In general, the positions showing anomalous RM with rapidly changing magnitude and sign are positions where noise dominates, so that reliable RM determination is not possible, see Sect. 4.

Contributions to the RM are made along the line of sight at positions with a non-zero electron density and magnetic field. This is the case in the warm and hot ISM components. The filling factor in the warm ISM is approximately 20% (Reynolds 1991), while the electron density in the hot ISM is so low that its RM contribution can be neglected for our purposes. Furthermore, polarized emission is increasingly depolarized when emitted at greater distances. Haverkorn et al. (2004a) estimate a distance of ~ 600 pc between observer and the ‘‘polarization horizon’’, defined as the point beyond which less than about a third of the polarized emission is not depolarized while propagating through the medium.

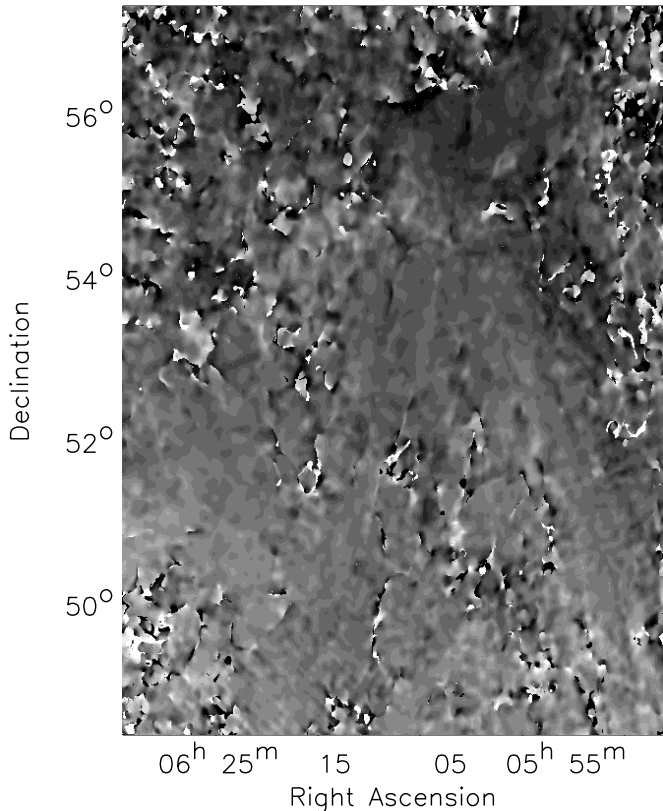


Fig. 2. Map of RM in the observed field. The grey scale runs from -15 to 15 rad m^{-2} . The map shows an RM value at every position, regardless of the quality of the linear fit of ϕ against λ^2 .

3. Numerical models

To estimate the effect of beam depolarization on the RM determinations, we generate artificial maps of polarized intensity at five wavelengths from numerical models of a turbulent magnetized ISM.

3.1. Domain considerations

Ideally, the numerical models should resemble the observational domain (i.e., the ratio between the length of the line of sight and the extent in the plane of sky) while retaining a resolution in the plane of sky comparable to the observations. At an estimated polarization horizon of 600 pc, the spatial extent of the $7^\circ \times 9^\circ$ field of observation is about 75 pc. The observational resolution of $4'$ would correspond to approximately 120×120 resolution elements in the plane of sky.

However, for the numerical models, this estimated requirement is too optimistic for two reasons. First, in order to investigate beam depolarization, we need substructure within one beam (i.e. resolution element). Second, any magnetohydrodynamics (MHD) code suffers from numerical dissipation at the smallest scales, thus introducing a lower limit for physically reasonable structures in the simulations (between 2 to 4 resolution elements in our case). Both requirements taken together lead to a desirable resolution of $\sim 500 \times 500$ elements in the plane of sky for the simulations, resulting in a domain size of

Table 1. Parameters of the numerical models used: N_x , N_y and N_z are the model dimensions in resolution elements and L_{los} is the length of the line of sight in parsecs. The initial magnetic field B_{\parallel} is oriented along the line of sight z and n_e is the initial uniform electron density. ΔRM is the width σ of the Gaussian distribution of RM , scaled via L .

name	$N_x \times N_y \times N_z$	L_{los} [pc]	B_{\parallel} [μG]	n_e [cm^{-3}]	ΔRM [rad m^{-2}]
<i>B1</i>	$512 \times 512 \times 4096$	100	2.5	0.1	3
<i>B2</i>	$512 \times 512 \times 4096$	200	2.5	0.1	6
<i>B3</i>	$512 \times 512 \times 4096$	400	2.5	0.1	10
<i>B4</i>	$512 \times 512 \times 4096$	600	2.5	0.1	15
<i>B5</i>	$512 \times 512 \times 4096$	800	2.5	0.1	25

$500 \times 500 \times 4000$ elements. This is beyond current computer capacities.

Thus we decided to use a cubic simulation domain (at 512^3 elements) and to construct a bar-like domain by stacking this cube 8 times, each time rotating it and shifting it by one fifth of the domain size. Thus we get different realizations of the turbulent structures, mimicking a turbulent medium over the whole length of the line of sight.

3.2. Model description

Our “observational” domain is derived from a periodic-box-simulation of the turbulent magnetized ISM by Li et al. (2000, 2004) and Heitsch et al. (2001), employing ZEUS-MP, the massively parallel version of ZEUS-3D (Norman 2000). The electron density and the magnetic field are rescaled to the values for the warm ISM, from which five models with different path lengths through the medium were constructed, as shown in Table 1.

The density and the magnetic field are initially uniform, and will be perturbed by a fixed velocity field. We generate the velocity field as described by Mac Low (1999), as follows. Each wave number k is given an amplitude in Fourier space, which is randomly drawn from a Gaussian distribution around unity, and a random phase. Fourier transforming to velocity space yields velocity components in three dimensions for each position. This is the velocity field with which the model is perturbed at each timestep, to simulate turbulent driving. The velocity components are multiplied by a velocity amplitude at each timestep, chosen such that the input energy stays constant with time. Perturbations are only induced at the lowest spatial wavenumbers $1 < k < 2$. In the plane of sky, this corresponds to the largest scales possible in the domain. The driving mechanism is meant to mimic energy input on the largest scales by an unspecified physical process such as supernova shock fronts or Galactic shear.

We use a snapshot of the simulation at a time when the full turbulent cascade has developed and a steady state between energy input on the largest scales and numerical dissipation on the smallest scales has been reached. This steady state corresponds to a Mach number of $\mathcal{M} \approx 10$. This is more than the values usually assumed for the warm ISM (namely $\mathcal{M} \approx 1$ at a

sound speed of $\approx 6 \text{ km s}^{-1}$), thus rendering the turbulence more compressive than intended for this work.

However, the turbulent cascade represented by a Kolmogorov slope of $-5/3$ does not change substantially (see e.g., Cho et al. 2003), so that we can rescale the densities and field strengths to values appropriate for the warm ISM. Fluctuations in electron density are allowed up to an upper limit of 10% of the mean density (assumed to be 0.1 cm^{-3}), which corresponds to the upper limit to structure in emission measure (EM) in the field of observation given by high-resolution $H\alpha$ observations (Madsen, private communication). The field variations are of the order of the mean field of $2.5 \mu\text{G}$.

We assume a filling factor of ionized gas of 100%, and a sharp cutoff of Faraday rotation of the polarized emission at 600 pc. As the RM is an integral over the line of sight, a smaller filling factor combined with a longer path length would give the same results.

The MHD model does not contain synchrotron emission within the medium itself. This is obviously not a realistic situation, but allows us to investigate the influence of beam depolarization without depth depolarization, as the latter only occurs in a medium that both Faraday rotates and emits. Including synchrotron emission in the medium would result in additional depolarization and larger deviations from the linear $\phi(\lambda^2)$ relation.

3.3. Simulating beam depolarization

The goal is to produce maps of Stokes Q and U from the models, which then can be treated like observational data. From the bars we construct the numerical RM in the plane of sky as

$$RM_{i,j} = 0.81 \frac{L_{\text{los}}}{N_z} \sum_{k=1}^{N_z} [n_e B_{\parallel}]_{i,j,k}, \quad i, j \in \{1 \cdots N_x\}, \quad (3)$$

in units of rad m^{-2} . The line-of-sight length L_{los} is given in parsecs, the electron density n_e in cm^{-3} , and the magnetic field component along the line-of-sight B_{\parallel} in μG . N_x, N_z are the number of cells in x and z direction, respectively, and $N_y = N_x$. For simplicity, we integrate along parallel lines of sight instead of an integration over a cone-like domain. Stokes Q_0 and U_0 are derived from those maps via

$$\phi = RM \lambda^2, \quad (4)$$

$$U_0 = \sin(2\phi), \quad (5)$$

$$Q_0 = \cos(2\phi). \quad (6)$$

Note that we assume 100% uniform background polarization, $P_0 = \sqrt{Q_0^2 + U_0^2} = 1$, and a constant background polarization angle of $\phi_0 = 0$. The wavelength λ is given in meters.

To mimic the limited telescope resolution, we smooth the Stokes Q_0 and U_0 maps with a Gaussian beam of width σ . This results in maps of Q and U which are σ times oversampled and which now can be used like observational maps. A noise level of $0.05 Q, U_{\text{rms}}$ is added to the Stokes parameters, which corresponds to the noise in the high signal-to-noise regions in the observations. P and ϕ are calculated according to Eqs. (1)

and (2). From the angle maps corresponding to the five observational wavelengths we finally can determine RM_{fit} as

$$\phi = RM_{\text{fit}} \lambda^2. \quad (7)$$

We apply the same criteria to select reliable fits as in the observations (see end of Sect. 2).

Figure 3 gives an example for model $B4$ at smoothing $\sigma = 4$. P shows elongated regions of depolarization, not directly related to features in the RM map. However, the regions of low polarized intensity P occur at locations of large gradients in RM . These structures reappear in the fitted RM , since regions of low P are noise-dominated and thus do not allow an accurate fit. The other models show similar characteristics: elongated depolarized regions which are one beam wide are present in all models, and the RM derived from smoothed data is patchy and shows sub-beam scale anomalies. However, a larger width of the RM distribution ΔRM induces more depolarization, so that larger depolarized regions exist in those models. For further distinction between models, see Sect. 5.

4. Depolarization canals

All high-resolution observations of the polarized intensity of the diffuse synchrotron background exhibit elongated, one-beam-wide ‘‘canals’’ of very low or zero P , where the radiation is depolarized (e.g., Duncan et al. 1997, 1999; Gray et al. 1999; Uyaniker et al. 1999; Gaensler et al. 2001; Haverkorn et al. 2003a,b). The polarization angle always changes by 90° across such a canal (Haverkorn et al. 2000). Two possible explanations exist for the depolarization canals (see e.g., Burn 1966; Sokoloff et al. 1998):

1. beam depolarization: if the gradient in $RM \nabla RM = (2n + 1)\pi/2$ within one beam, the radiation within the beam is depolarized. This mechanism would explain the fact that canals do not shift in position with frequency. However, it requires a medium with steep gradients in RM and/or intrinsic angle ϕ_0 within one beam, elongated perpendicularly to the gradient;
2. depth depolarization: a uniform synchrotron emitting magneto-ionic medium can cause complete depolarization for $|RM| = n\pi$. However, in this explanation the depolarization canals shift in position with frequency, and a uniform medium (across a major part of the path length) is needed for complete depolarization.

Haverkorn et al. (2004b) argue that in their observations (one of which is used here), beam depolarization due to RM gradients is the dominant mechanism causing depolarization canals. This does not in any way mean that depth depolarization is not important in the rest of the medium. For observations made at 350 MHz, only a modest gradient in RM across a beam ($\sim 2.1 \text{ rad m}^{-2}$) can create a canal, whereas much larger gradients ($\sim 34 \text{ rad m}^{-2}$) are needed to form a canal in 1.4 GHz observations. For an interpretation of canals at 1.4 GHz in terms of depth depolarization, see Shukurov & Berkhuijsen (2003).

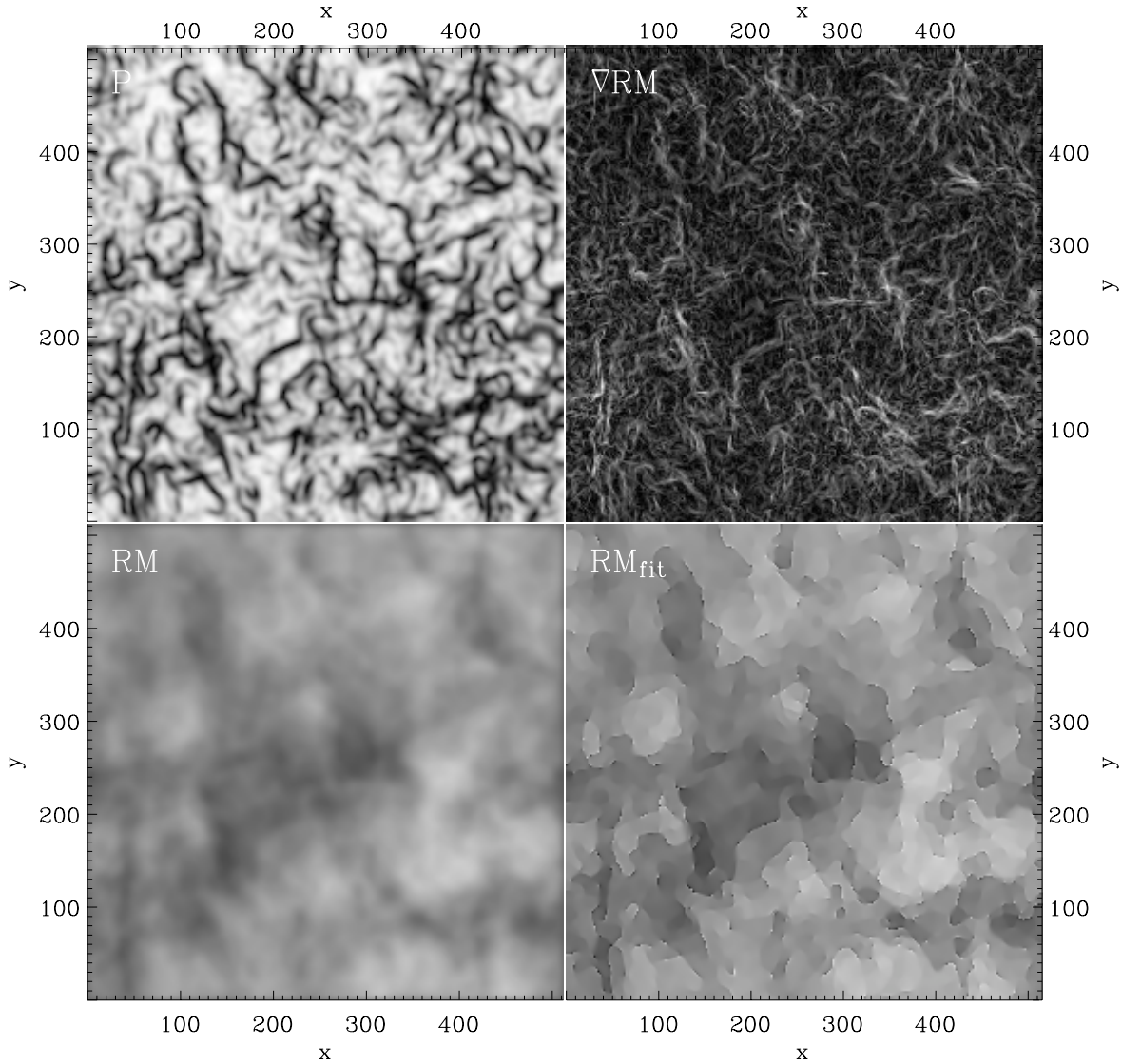


Fig. 3. Polarized intensity P ($4 \times 10^{-3} < P < 0.97$), gradient of RM , $|\nabla RM|$ ($1 \times 10^{-3} < |\nabla RM| < 4.9 \text{ rad m}^{-2} \text{ pixel}^{-1}$) and numerical and fitted RM (scaled identically between $-6.8 < RM < 22.32 \text{ rad m}^{-2}$) for model $B4$ at smoothing $\sigma = 4$, four times oversampled. Note that depolarized (black) canals appear at the locations of large (white) gradients. These regions reoccur in anomalous RM_{fit} , leading to fringes in the fitted RM map.

In the numerical models discussed in Sect. 3, depolarization canals are visible as well (see top left map in Fig. 3), which are caused by beam depolarization.

At first sight, there is no obvious connection between the locations of the canals and RM (left hand maps in Fig. 3). However, the magnitude of the gradient in RM (top right map in Fig. 3) is obviously correlated to the position of the canals. This is demonstrated more quantitatively in Fig. 4, which shows a scatter plot of P against the magnitude of the gradient in RM with smoothing $\sigma = 4$ for each independent “beam”. The solid line denotes the theoretically expected depolarization in a beam due to a resolved gradient dRM/dr in RM (Sokoloff et al. 1998)

$$\frac{P}{P_0} = \exp \left[-\frac{1}{\ln 2} \left(\frac{dRM}{dr} \right)^2 \lambda^4 \right] \quad (8)$$

where P_0 is the polarized intensity for constant RM within the beam. The polarized intensity decreases almost to zero where the gradient in RM is such that $\Delta\phi \approx \pi/2$.

We selected “canal-like beams” by comparing P in a certain point to the average P of two diametrically opposed neighboring beams. If P in the central beam was less than 20% of the averaged P of the neighboring beams, the beam was considered a canal. Note that this selection criterion does not use any information about the length of the canals. Figure 5 shows the distribution of the gradient in RM only at canals, defined according to the above process. The five plots show canals defined in five wavelengths, and the solid and dotted lines represent smoothings $\sigma = 4$ and 8, respectively. The dashed lines denote the value of ∇RM at the location where $\Delta\phi = -\pi/2, \pi/2$. Clearly, the gradient in RM is peaked at the value where $\Delta\phi = \pi/2$. The decline in number of canal pixels with frequency can be explained by the fact that the width

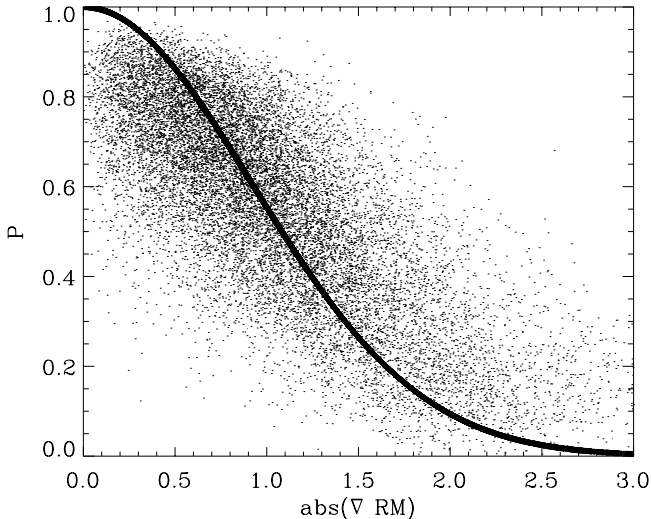


Fig. 4. Absolute value of the gradient in original RM in the simulations $|\nabla RM|$ against polarized intensity P of the smoothed maps with smoothing $\sigma = 4$ for each pixel. The curve corresponds to Eq. (8).

of the polarization angle distribution decreases with increasing frequency for a given RM distribution.

So the gradient of RM in the canals has the right magnitude to cause beam depolarization (Fig. 5). Since the canals exist over many beams, the most likely direction of this gradient is perpendicular to the direction of the canals. In Fig. 6 we show P in grey scale, with vectors of the RM gradient superimposed, demonstrating that indeed the gradients in RM are directed perpendicular to the canals.

Detailed analysis of the shape, direction and origin of RM gradients and the implications on the medium will be discussed in a forthcoming paper. However, we give a simple estimate here of the required changes in magnetic field strength B and/or electron density n_e to produce large enough gradients. For $\lambda = 0.80$ m, $\Delta RM = 2.45$ rad m⁻² in order to get an angle change of $\Delta\phi = \pi/2$ within a beam. If the structures in ∇RM are filaments at an average distance of 300 pc, their width would be 0.4 pc. The necessary ΔRM requires an enhancement of n_e and B of a factor 3 to 4, for ISM parameters as in e.g. model B2 (see Table 1). On the other hand, if the structures are sheetlike, and have an extent along the line of sight of a few parsecs, then an increase in electron density and magnetic field of 50% is sufficient, or an increase in either n_e or B of 100%. However, the unpublished H α measurements discussed above (Madsen, private communication) give an upper limit to small-scale structure in emission measure $EM = \int n_e^2 dl \approx 0.3$ cm⁻⁶ pc, which corresponds to a maximum $\Delta n_e \approx 0.02$ cm⁻³. Therefore, the gradients in RM are probably mainly caused by magnetic field changes, and could originate from shocks, local narrow magnetic field reversals or other sheet-like structures in density and/or magnetic field.

Note that the canals in the numerical models are much shorter and less ordered than the ones in the observations. This is because in the numerical models we can introduce dynamical structure self-consistently only up to the domain size. Ideally, we would like to use subframes from the numerical models to

be able to include larger scale structure in the models, so that modeling of canals across a significant part of the field would be possible. However, the available resolution is too low for this to be feasible.

Elongated narrow gradients in magnetic field and/or density have also been seen in other numerical simulations (e.g., Schekochihin et al. 2002; Cho et al. 2002).

Thus, in the numerical models discussed here, narrow and elongated gradients in RM exist of large enough magnitude to cause beam depolarization in the modeled medium. Taking into account other observational evidence (Haverkorn et al. 2004b), this leads us to conclude that the narrow and deep depolarization canals as seen in the observations are most likely caused by beam depolarization due to RM gradients.

5. Reliability of RM determinations

The beam depolarization raises the issue of how reliable the RM determinations are. Figure 7 quantifies the effect of limited resolution on the values of the computed RM . We determine the normalized mean quadratic difference between fitted and original smoothed RM as

$$\delta RM = \left(\frac{\langle (RM_\sigma - RM_{\text{fit}})^2 \rangle}{\langle RM^2 \rangle} \right)^{1/2}, \quad (9)$$

where RM is the original RM and RM_σ is RM smoothed over Gaussian beams of width σ . We have chosen δRM defined by Eq. (9) for the following reason. The goal of the equation is to compare the fitted RM to the “real” RM in the modeled medium. On scales below the beam size, the fitted RM by definition cannot show any structure that represents structure in the medium. Therefore, if RM_{fit} would be compared to the RM as directly derived in the model, $RM_{\text{fit}} - RM$ would give large values which are not the result of the smoothing, but only due to the fact that the beam size is incorporated in the determination of RM_{fit} , but not in that of RM . Therefore, we chose to compare RM_{fit} to an RM which is smoothed over a Gaussian beam, assuming that the smoothed RM approximates the physical RM in the model if viewed only on scales larger than the beam size. In addition, the subsequent normalizing to the distribution width of the original *unsmoothed* RM rules out any spurious effects on the difference estimates due to averaging. In this way, δRM is a measure of how accurately the RM computed from Q and U data with a finite beam width approximates the physical RM in the medium.

Figure 7 shows the deviations δRM for all independent beams satisfying the criteria for good fits (see end of Sect. 2). For a width of the RM distribution $\Delta RM \approx 20$ rad m⁻² and a smoothing of $\sigma = 4$ (values which are typical for the observations by Haverkorn et al. 2003a,b) we would expect from Fig. 7 an error of $\sim 20\%$ in the fitted RM . However, as we will see below, this error estimate is an upper limit.

For ΔRM small enough not to lead to sign changes of Q and U within a beam, the differences δRM saturate at a 5%-level with increasing beam width, since variations of RM within a beam are limited (Fig. 7 for $\Delta RM = 3$). This behavior changes profoundly if Stokes Q and U reverse sign

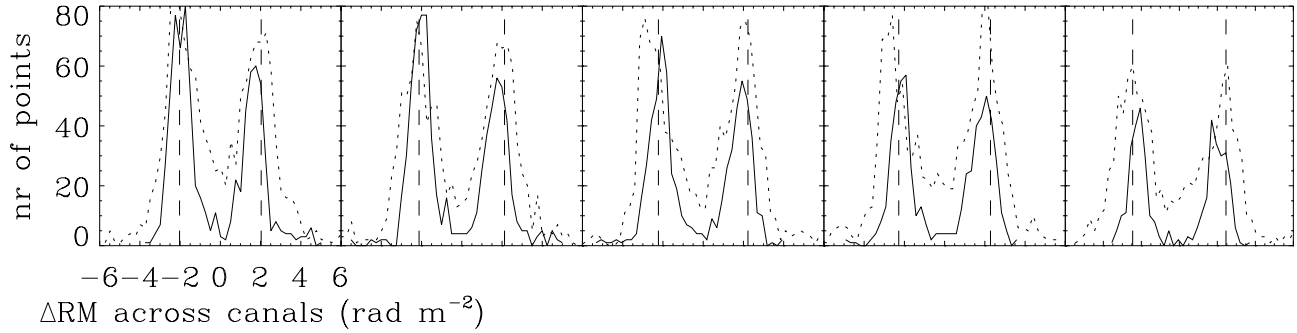


Fig. 5. Distribution of difference in RM across a canal, ΔRM . From left to right, canals are selected in wavelengths of 88 cm, 86 cm, 84 cm, 83 cm and 80 cm, respectively. The solid line denotes canals in P maps smoothed by $\sigma = 4$, the dotted lines are for a smoothing $\sigma = 8$. The dashed lines give the positions where $\Delta RM\lambda^2 = -\pi/2, \pi/2$.

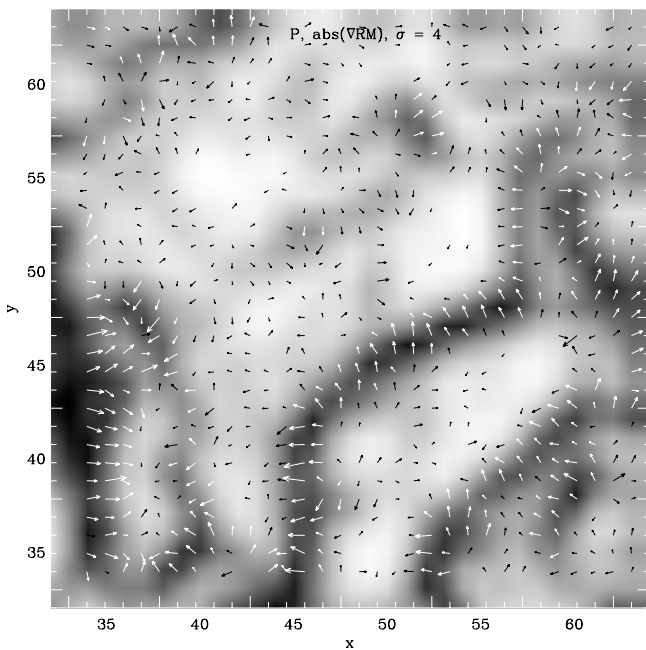


Fig. 6. Part of the polarized intensity map at smoothing $\sigma = 4$ in grey scale, with strength and direction of the gradient in RM superimposed as vectors.

within one beam. This is equivalent to a change in polarization angle of 90° which, as discussed above, leads to depolarization canals. The effect on δRM is twofold:

1. Low P means small S/N , thus not well defined angles, and thus large errors in the fits. Therefore, those fits are excluded by the selection criterion.
2. Averaging introduces slight non-linearities in the angles around depolarized regions, i.e. regions where Stokes Q and U reverse sign within one beam. These non-linearities lead to an overshoot of the RM (see Fig. 8) close to the depolarized region.

With increasing ΔRM , Stokes Q and U are more likely to change sign within a beam. Beam averaging then leads to much severer depolarization (see Fig. 8). Depolarized regions are accompanied by systematic overshoots in RM_{fit} (Fig. 8, top panel), which stem from the non-linearities in Eq. (2) arising when Stokes Q changes sign. (Note that in the bottom panel

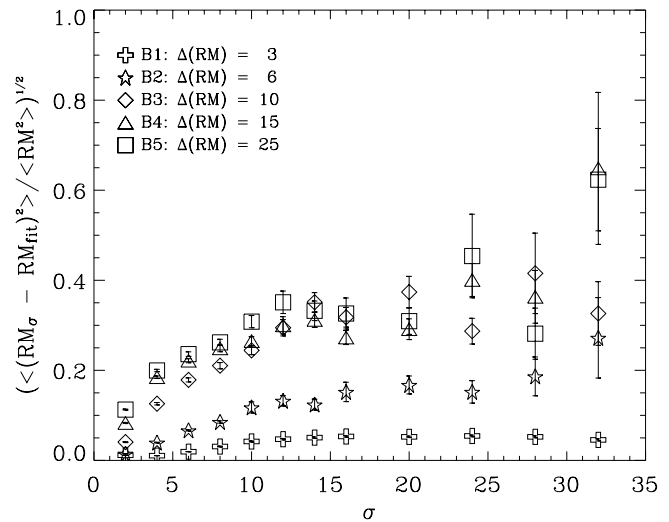


Fig. 7. Deviation of RM , δRM , calculated from smoothed Q and U maps from original RM , relative to original RM , against smoothing σ (see Eq. (9)). Different symbols denote results for models B1 to B5 with a given width of the original RM distribution. Only independent beam positions with $(P > 5 S/N) \wedge (\chi^2 < 2)$ are used to determine δRM .

of Fig. 8, the polarization angles derived from beam-averaged Stokes Q and U are not ordered with respect to λ any more in a canal, thus leading to ill-defined fits.) The overshoots of extreme positive and negative RM are also visible in the observational data (see Fig. 2), indicating that the depolarization canals in the data are also caused by beam depolarization as opposed to depth depolarization.

Not all RM gradients introduce these spurious results. Far away from the gradient, the fits retrieve the original RM . However, close to the gradient, multiple oscillations of Q_0 and U_0 within the gradient lead to Q and U close to zero over an extended region.

For one isolated RM -gradient as shown in Fig. 8a (see figure caption), the differences δRM selected for reliable fits behave with the change in RM across the canal ΔRM as shown in Fig. 9. The first spike corresponds to a 0th order canal with an angle difference of $\pi/2$. Higher-order canals have angle differences of $(2n + 1)\pi/2$, as discussed above. The RM field from

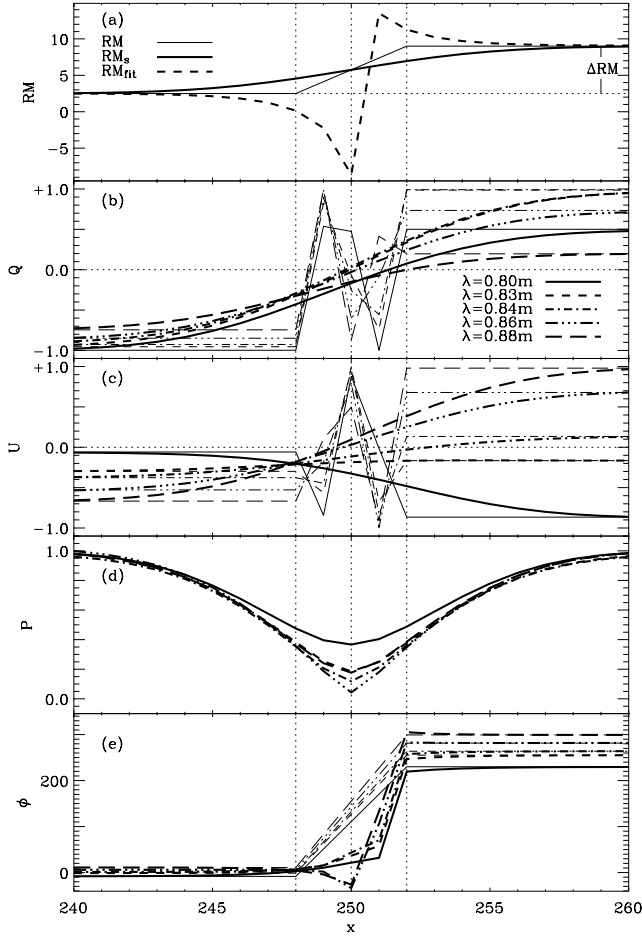


Fig. 8. Details of an idealized canal caused by sign changes in Stokes Q (see text). **a)** RM against spatial coordinate x . The original RM (thin line) has a gradient between the two vertical dotted lines, leading to a smoothed RM_s (thick solid line) and a fitted RM_{fit} (thick dashed line) showing an overshoot, as in the observations. Smoothing (“beam”) width corresponds to $\Delta x = 4$. ΔRM as used in the text is the change of RM over the gradient, in this case $\Delta RM = 6.5$. **b)–d)** Stokes Q , U and polarized intensity P for all wavelengths before smoothing (thin lines) and after smoothing (thick lines): strong oscillations of the unsmoothed Q and U within the gradient region of RM (see Eqs. (5) and (6)) lead to cancellation of smoothed Q and U within that region. Correspondingly, P drops to nearly 0. **e)** polarization angles for all wavelengths (as denoted in legend of Q). Thin lines show the angles derived from the original, unsmoothed RM , thick lines denote the angles derived from the smoothed Q and U . Note that within the gradient region, there is no ordering of ϕ with λ .

the numerical models is a combination of all ΔRM s given in Fig. 9.

Note that the fitted RM_{fit} deviates from the original RM most for those RM gradients where canals occur. In between the spikes, at positions where canals are not near, the difference δRM drops nearly to zero, i.e. a finite beam width has almost no effect on the RM determination. Therefore, δRM is dominated by values around canals where $P > 5 S/N$ (needed to be selected as reliable RM).

From Fig. 9 we conclude that the difference estimates δRM for $\Delta RM > 3 \text{ rad m}^{-2}$ as given in Fig. 7 are indeed too pessimistic, since they are dominated by the regions around canals,

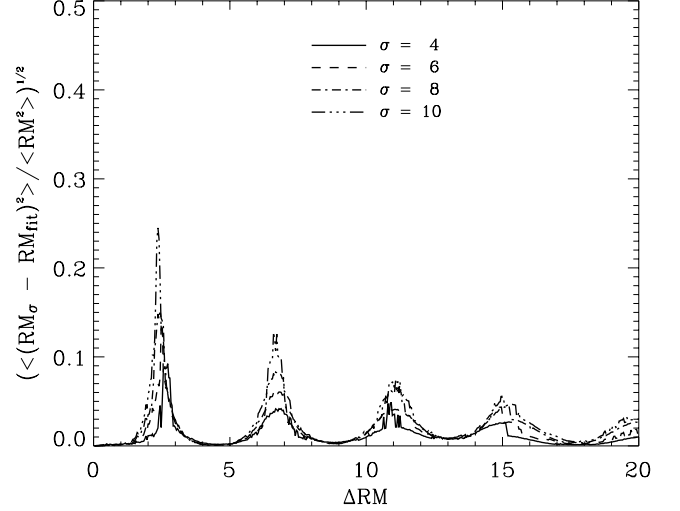


Fig. 9. δRM (see Eq. (9)) for an isolated RM -gradient as shown in Fig. 8a against ΔRM , the change of RM across the gradient. The gradient width is 4 pixels while the beam width varies between 4 and 10 pixels. Fitted RM s are derived in the same way as for the models, selected for $(P > 5 S/N) \wedge (\chi^2 < 2)$ and independent beams. Note the periodicity $T_{RM} \approx 4.4$ in δRM , corresponding to an angle change of π . The first spike occurs at an angle difference of $\pi/2$, the canal of 0th order.

that are influenced by the canals but still fall within the definition of “reliable RM s”. For smooth regions, or regions not affected by canals, we expect the RM s determined from the observations to be accurate within 5% of ΔRM , corresponding to an error of 0.15 rad m^{-2} for the observations mentioned here. The overall error will increase with increasing number of canals, which is why Fig. 7 generally shows larger δRM than Fig. 9.

6. Conclusions

Multi-frequency radio observations of the Galactic synchrotron background allow us to probe the structure of the magneto-ionized component of the ISM from RM maps. However, the quality of the RM determinations depends strongly on the degree of local depolarization due to intrinsic structure in the ISM, and thus in the RM . We investigated the effect of beam depolarization on the quality of the fitted RM s with the help of numerical models. We find:

1. The models show depolarization canals due to beam depolarization across sharp gradients in RM . This suggests that narrow gradients of a few rad m^{-2} can be a common feature in a magneto-ionized medium. Combined with other observational evidence, we therefore conclude that the depolarization canals seen in our 350 MHz observations are caused by beam depolarization due to RM gradients. While the width of the canals is an observational artifact, their presence and length mirror underlying structure in the Faraday-rotating medium.
2. RM determinations close to canals can be incorrect by several rad m^{-2} , depending on the absolute RM difference between both edges of the canal. This is a consequence of a non-linearity in $\phi(\lambda^2)$ introduced by finite beam width.

3. RM determinations in smooth regions or in regions separated from canals by at least a beam are accurate to $0.05\Delta RM$, where ΔRM is the width of the RM distribution, or $\delta RM = 0.15 \text{ rad m}^{-2}$ for the observations mentioned here.

In future research, improved models will enable us to investigate what structures in the ISM actually cause the elongated gradients of RM , and will serve as a calibration what information about structure we can extract from observational maps.

Acknowledgements. The authors wish to thank Ellen Zweibel, Peter Katgert, Mordecai-Mark Mac Low and Enrique Vázquez-Semadeni for enlightening and invigorating discussions. We are grateful to P. S. Li and M. L. Norman for making the 512³ available, and thank Wolfgang Reich for useful and critical comments. Computations were performed on the SGI Origin 2000 of the National Center for Supercomputing Applications (NCSA) at Urbana-Champaign. The Westerbork Synthesis Radio Telescope is operated by the Netherlands Foundation for Research in Astronomy (ASTRON) with financial support from the Netherlands Organization for Scientific Research (NWO). The project originated during the Astrophysical Turbulence Program at the KITP at University of California, Santa Barbara in 2000 (NSF grant PHY94-07194). M.H. is supported by NWO grant 614-21-006. F.H. is supported by a Feodor-Lynen fellowship of the Alexander-von-Humboldt Foundation and by NSF grant AST-0098701.

References

- Armstrong, J. W., Rickett, B. J., & Spangler, S. R. 1995, *ApJ*, 443, 209
- de Avillez, M. A., & Mac Low, M.-M. 2002, *ApJ*, 581, 1047
- Burn, B. J. 1966, *MNRAS*, 133, 67
- Cho, J., Lazarian, A., & Vishniac, E. T. 2002, *ApJ*, 564, 291
- Cho, J., Lazarian, A., & Vishniac, E. T. 2003, *ApJ*, 595, 812
- Crutcher, R. M. 1999, *ApJ*, 520, 706
- Duncan, A. R., Haynes, R. F., Jones, K. L., & Stewart, R. T. 1997, *MNRAS*, 291, 279
- Duncan, A. R., Reich, P., Reich, W., & Fürst, E. 1999, *A&A*, 350, 447
- Gaensler, B. M., Dickey, J. M., McClure-Griffiths, N. M., et al. 2001, *ApJ*, 549, 959
- Gray, A. D., Landecker, T. L., Dewdney, P. E., et al. 1999, *ApJ*, 514, 221
- Haverkorn, M., Katgert, P., & de Bruyn, A. G. 2000, *A&A*, 356, L1
- Haverkorn, M., Katgert, P., & de Bruyn, A. G. 2003a, *A&A*, 403, 1031
- Haverkorn, M., Katgert, P., & de Bruyn, A. G. 2003b, *A&A*, 404, 233
- Haverkorn, M., Katgert, P., & de Bruyn, A. G. 2004a, *A&A*, submitted
- Haverkorn, M., Katgert, P., & de Bruyn, A. G. 2004b, *A&A*, submitted
- Heitsch, F., Zweibel, E. G., Mac Low, M.-M., Li, P. S., & Norman, M. L. 2001, *ApJ*, 561, 800
- Larson, R. B. 1981, *MNRAS*, 194, 809
- Li, P. S., Norman, M. L., Heitsch, F., & Mac Low, M.-M. 2000, *BAAS*, 197, 502
- Li, P. S., Norman, M. L., Mac Low, M.-M., & Heitsch, F. 2004, *ApJ*, accepted
- Mac Low, M.-M. 1999, *ApJ*, 524, 169
- Mac Low, M.-M., & Klessen, R. 2003, *ARA&A*, in press [arXiv:astro-ph/0301093]
- Minter, A., & Balsaer, D. S. 1998, *LNP*, 506, 543
- Norman, M. L. 2000, *Rev. Mex. Astron. Astrofis. Conf. Ser.*, 9, 66
- Reynolds, R. J. 1991, *ApJ*, 372, 17L
- Schekochihin, A. A., Maron, J. L., Cowley, S. C., & McWilliams, J. C. 2002, *ApJ*, 576, 806
- Sellwood, J. A., & Balbus, S. A. 1999, *ApJ*, 511, 660
- Shukurov, A., & Berkhuijsen, E. M. 2003, *MNRAS*, 342, 496
- Sokoloff, D. D., Bykov, A. A., Shukurov, A., et al. 1998, *MNRAS*, 299, 189
- Uyaniker, B., Fürst, E., Reich, W., Reich, P., & Wielebinski, R. 1999, *A&AS*, 138, 31